PIER C

Simulation Research on Breast Tumor Model Based on Magnetoacoustic Concentration Tomography of Magnetic Nanoparticles with Magnetic Induction

Xiaoheng Yan[1, 2], Fangtian Liu[1, *], Waldemar T. Smolik[3], Xinxian Dan[1], and Xiaohan Hou[1]

[1]*Faculty of Electrical and Control Engineering, Liaoning Technology University, Huludao 125000, China*
[2]*The Belt and Road Joint Laboratory on Measurement and Control Technology*
Huazhong University of Science and Technology, Wuhan 430074, China
[3]*Faculty of Electronics and Information Technology, Warsaw University of Technology, Warsaw, Poland*

ABSTRACT: Magnetic nanoparticles (MNPs) have been widely investigated as effective drug carriers for targeted tumor therapy. However, the successful application of this technology in the human body requires reliable imaging support. Magnetoacoustic Concentration Tomography of Magnetic Nanoparticles with Magnetic Induction (MACT-MI) is an electromagnetic-ultrasonic coupling imaging technique that holds great promise in improving imaging resolution and providing unique advantages for tumor monitoring and treatment. To evaluate the imaging feasibility of MACT-MI technology for targeted therapy of breast tumors, this study establishes a realistic breast model and takes into account the distribution of magnetic particles within the actual breast tissue environment. A concentration gradient model is introduced, and the finite element method is employed to solve the electromagnetic and sound fields. In addressing the research objective, the forward problem is investigated by analyzing the magnetic force and sound pressure distribution for various tumor sizes and locations, different breast tissues, and both benign and malignant tumors. The results obtained indicate that the magnetoacoustic signal emitted by magnetic particles facilitates accurate mapping of the size and location information of magnetic particles enveloping breast tumors, as well as distinguishing between benign and malignant tumors.

1. INTRODUCTION

Superparamagnetic nanoparticles (MNPs) have emerged as a promising technology that has the potential to revolutionize diagnostic and clinical treatment approaches, thanks to their favorable characteristics such as excellent biodegradability, micro-size effect, and magnetic properties [1, 2]. In recent years, extensive research has been conducted by scholars worldwide on the use of magnetic particles for targeted drug delivery. Notably, Yang et al. [3] and Taherian et al. [4] investigated the application of magnetic nanoparticles in breast cancer treatment, demonstrating significant improvements in therapeutic efficacy. They confirmed that magnetic nanoparticles exhibit minimal cytotoxicity to cells while enabling accumulation and long-term retention at the tumor site under magnetic guidance. In targeted drug delivery systems, MNPs can be guided and directed to specific tissues using an external magnetic field. However, to ensure precise magnetic localization, an imaging navigation system is essential to provide technical support. Magnetic particle imaging (MPI) has emerged as a crucial imaging technique for the medical application of MNPs, enabling real-time three-dimensional imaging of the nonlinear magnetization induced by MNPs in the presence of an external oscillating magnetic field. MPI offers high sensitivity, excellent contrast, and negligible depth signal attenuation, making it widely utilized in various biomedical clinical imaging scenar-

ios [5]. Furthermore, MPI allows imaging of any region of the body without subjecting patients to ionizing radiation, thus ensuring their safety. Previous studies have already demonstrated the potential of MPI in cell tracking, tumor imaging, and vascular imaging [6–8]. However, the current spatial and temporal resolution of 0.5 mm in magnetic particle imaging is believed to have reached a theoretical upper limit, presenting a challenging bottleneck for further advancements in this field. Efforts to overcome this limitation and achieve higher resolution are ongoing but continue to pose significant challenges.

Magnetoacoustic Concentration Tomography of Magnetic Nanoparticles with Magnetic Induction (MACT-MI) is an innovative method for targeted therapy that has been recently proposed. It combines the advantages of electromagnetic and ultrasonic technologies, offering non-invasiveness, excellent contrast, high sensitivity, and quantitative estimation of magnetic nanoparticles. These features contribute to improved imaging resolution. The concept of MACT-MI was first introduced by Shi et al. in 2020, enabling the imaging of magnetic nanoparticle concentrations [9]. In the same year, Yan et al. presented an MACT-MI imaging method under saturated magnetization, investigating the forward problem and demonstrating that saturated magnetization enhances the magnetoacoustic signals produced by magnetic nanoparticles [10]. Consequently, MACT-MI holds great potential for tumor targeted therapy. Breast cancer represents the most prevalent form of cancer worldwide. In 2020, there were over 2.3 million new cases and 685,000 deaths

---

reported [11]. The modern approach to breast cancer surgery aims to minimize surgical intervention while ensuring tumor safety. In this regard, Jung et al. developed a novel therapeutic diagnostic platform utilizing hypoxic exosomes for delivering anticancer drugs and radiosensitizers to hypoxic cancers. Monitoring of treatment effects was achieved through magnetic particle imaging (MPI) [12]. Wang et al. designed an intelligent detection imaging probe targeting breast tumors and combined it with the imaging advantages of MPI to detect lymph node metastasis in breast cancer [13]. Parkins et al. successfully visualized circulating tumor cells (CTCs) loaded with superparamagnetic iron oxide in breast cancer mice using high-sensitivity MPI. This groundbreaking study demonstrated MPI's capability to sensitively detect iron-labeled CTCs and visualize tumor homing in breast cancer mice [14]. Zhu et al. developed a superparamagnetic core-shell nanocomposite as a drug delivery system and MPI quantitative tracer. In vivo drug release monitoring was achieved using a mouse breast cancer model, enabling visualization of drug release and spatial distribution through MPI imaging [15]. These studies collectively highlight the advantages of MPI in breast cancer targeted therapy.

To further enhance the imaging resolution of magnetic particles in the field of breast targeted therapy, our research group investigated the feasibility of MACT-MI technology in this domain. In this paper, we conducted simulation analyses of a breast tumor model based on MACT-MI theory. We constructed a realistic breast model and established simulation models for various breast tumor sizes, locations, different breast tissue types, and malignant tumors. Through finite element numerical calculations, we solved the forward problem of MACT-MI and analyzed the distribution of magnetic force and sound pressure for different models. The results confirmed the feasibility of MACT-MI technology for breast tumor monitoring and targeted therapy.

2. METHOD

As depicted in Figure 1, the MACT-MI technique involves the injection of MNPs into biological tissues, followed by the application of a static magnetic field generated by a cylindrical permanent magnet and a z-direction time-varying magnetic field produced by a Maxwell coil. Upon magnetization, the MNPs interact with the time-varying magnetic field, resulting in magnetic vibrations that generate ultrasonic waves. The varying concentrations of MNPs within the biological tissues lead to different magnetic forces, subsequently resulting in distinct sound pressures. These sound pressure signals, which contain concentration information, are detected by a rotating ultrasonic transducer. By leveraging the nonlinear relationship between the sound pressure data and the concentration of MNPs, the concentration distribution image is reconstructed using the time reversal method and finite difference method.

In the MACT-MI forward problem, the time-varying external magnetic field applied by the Maxwell coil-cylindrical permanent magnet system is:

$$\mathbf{B}_z = \mathbf{B}_{sat} + \mathbf{B}_g \qquad (1)$$

where $\mathbf{B}_{sat}$ is a static magnetic field generated by a cylindrical permanent magnet, and the magnetic field generated by the permanent magnet is constant, which is used to make the magnetic nanoparticles reach a saturated magnetization state. $\mathbf{B}_g$ is the gradient magnetic field generated by the Maxwell coil and is a function of time and space, as shown in Formula (2):

$$\mathbf{B}_g(r,t) = \mathbf{B}_g(r)\,s(t) \qquad (2)$$

where $\mathbf{B}_g(r)$ is the spatial distribution of the gradient magnetic field, and $s(t)$ is its time term.
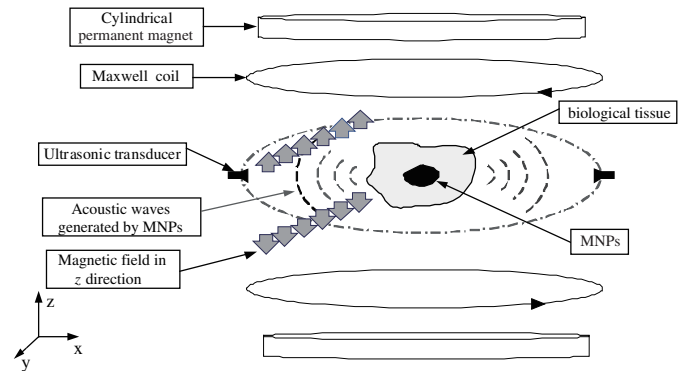

FIGURE 1. MACT-MI imaging principle.

In general, the saturation magnetic field strength is defined as the field strength at which the magnetization of the MNPs solution reaches 80% of its saturation magnetization. The expression for saturation magnetic field strength is given by:

$$H_{\mathrm{s}} = \frac{5\,kT}{\mu_0 m} \qquad (3)$$

where k is the Boltzmann constant; T is the temperature, and unit is Kelvin; μ_0 is the vacuum permeability; m is the inherent magnetic moment of magnetic particles.

When the magnetic field intensity generated by the cylindrical permanent magnet exceeds a certain threshold, denoted as H_{s}, the magnetic nanoparticles within the imaging area become saturated.

Given the diffuse and gradual concentration distribution of MNPs in actual breast tissue, this study establishes a concentration gradient model for MNPs in breast detection, which better reflects the real scenario within the human body. In this paper, the average concentration of MNPs is set to be the same in both the concentration gradient model and the uniform concentration model. Specifically:

$$N_0 = \frac{\iiint_\Omega N(x,y,z)\,dV}{V} \qquad (4)$$

Here, N_0 represents the number concentration of MNPs in the uniform concentration model, while $N(x,y,z)$ represents the concentration distribution formula of MNPs in the concentration gradient model.

In the gradient model established in this study, the concentration of MNPs varies radially, and it can be denoted as
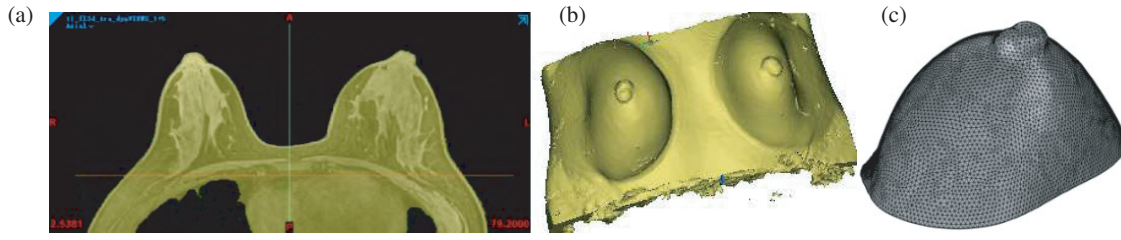
FIGURE 2. (a) Organization mask; (b) Three-dimensional model of tissue; (c) Breast model.

$N(x, y, z)$:

$$N(x,y,z) = \begin{cases} \left(r_2 - \sqrt{(x-x_0)^2 + (y-y_0)^2 + (z-z_0)^2}\right) \times N_0, \\ \qquad\qquad\qquad\qquad\qquad\qquad r_1 < |R| \le r_2 \\ 2 \times N_0, \qquad\qquad\qquad\quad |R| \le r_1 \\ 0, \qquad\qquad\qquad\qquad\quad |R| > r_2 \end{cases} \tag{5}$$

where $|R| = \sqrt{(x-x_0)^2 + (y-y_0)^2 + (z-z_0)^2}$, x, y, and z are the coordinate components in the Cartesian coordinate system, and the unit is mm. According to formula (4), (x_0, y_0, z_0) is the center of the tumor; r_1 is the width of the uniform concentration area; r_2 is the radius of the tumor. In this paper, $r_1 = 0.4 \times r_2$ is selected [16].

When the magnetic nanoparticles reach saturation magnetization under static magnetic field $\mathbf{B}_{sat}$, the magnetic force on MNPs can be described as [11]:

$$\mathbf{f}(\mathbf{r}, t) = Nm \frac{\partial B_g(r)}{\partial z} s(t) \mathbf{e}_z \tag{6}$$

where $\mathbf{f}(\mathbf{r}, t)$ represents that the magnetic force is a function of time and space; m is the inherent magnetic moment of magnetic particles $B_g(r)$ is the spatial distribution of the gradient magnetic field; the time term $s(t)$ of the external magnetic field is also the time term of the magnetic force. N is the number of MNPs per unit volume, that is, the concentration of MNPs, $\partial B_g(r)/\partial z$ is the gradient magnetic field in the z direction, and $\mathbf{e}_z$ is the unit vector in the z direction.

In the MACT-MI technique, utilizing the Maxwell coil-cylindrical permanent magnet gradient magnetic field system, the effective linear sound pressure wave equation remains applicable. In this system, the particles can be considered as acoustic dipoles, while the breast tissue medium can be treated as a non-viscous liquid [17, 18]. The sound pressure wave equation can be expressed as follows:

$$\nabla^2 p(\mathbf{r}, t) - \frac{1}{c^2} \frac{\partial^2 p(\mathbf{r}, t)}{\partial t^2} = \nabla \cdot \mathbf{f}(\mathbf{r}, t) \tag{7}$$

where r is any point in unbounded space, $p(\mathbf{r}, t)$ the spatial and temporal distribution of sound pressure field, c the sound velocity in biological tissue, $\mathbf{f}(\mathbf{r}, t)$ the magnetic force of MNPs, and the magnetic divergence $\nabla \cdot \mathbf{f}$ is the sound source term.

The moment when the Maxwell coil is energized is the initial moment. At this time, there is no gradient magnetic field in the imaging area, that is, $\partial B_g(r)/\partial z = 0$, and MNPs are not magnetic, that is, there is no sound source. Then, the forward sound field problem of MACT-MI in Maxwell coil-cylindrical permanent magnet system can be expressed as:

$$\begin{cases} \nabla^2 p(\mathbf{r}, t) - \frac{1}{c^2} \frac{\partial^2 p(r, t)}{\partial t^2} = \nabla \cdot \mathbf{f}(\mathbf{r}, t) \\ p|_{t=0^-} = 0 \\ \left. \frac{\partial p}{\partial t} \right|_{t=0^-} = 0 \end{cases} \tag{8}$$

3. MODEL

3.1. Construction of Breast Model

In this study, a three-dimensional geometric model of the breast is constructed using Mimics software and Geomagic software based on breast MRI tomography images. The following steps were undertaken: (1) The MRI breast tomography image data were imported; (2) The imported original breast MRI sequence diagram was processed using Mimics software, where a suitable gray threshold was selected to generate a mask and a three-dimensional model of the breast skin tissue; (3) The model exported by Mimics was further refined and meshed using Geomagic software to generate a model suitable for simulation in COMSOL software, as illustrated in Figure 2.

3.2. Imaging System

In order to reduce the amplitude of the excitation source and enable the MNPs to reach a saturated state, this paper selected the Maxwell coil-cylindrical permanent magnet system [9, 10, 19], as shown in Figure 3. The gradient magnetic field distribution of this magnet system within the imaging area of $100\,\text{mm} \times 100\,\text{mm}$ in the XOZ plane is presented in Figure 4. Previous studies [18] have indicated that the research on MACT-MI is conducted under gradient magnetic fields ranging from 0.1 T/m to 0.3 T/m. Hence, the magnet system employed in this study satisfies the imaging requirements of MACT-MI.

The relevant parameters of the cylindrical permanent magnet are summarized in Table 1. In the COMSOL software, the center of the magnet system is aligned with the z-axis. The remanence of the permanent magnet is set to 1.4 T, and the relative permeability is set to 0.9. These parameters are employed to simulate the magnetic field of the magnet model.

The Maxwell coil is made of metal copper, and its structural parameters are presented in Table 2. In this study, the
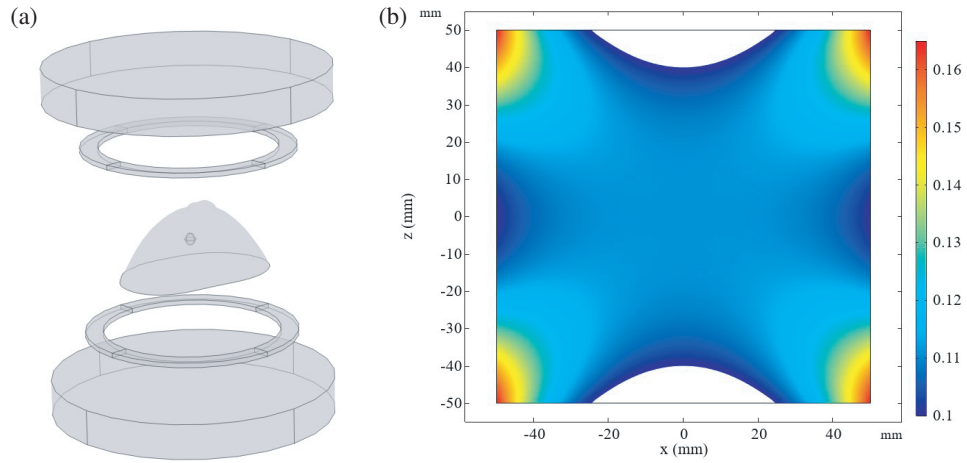
FIGURE 3. (a) MACT-MI simulation model; (b) Gradient magnetic field distribution in imaging area.
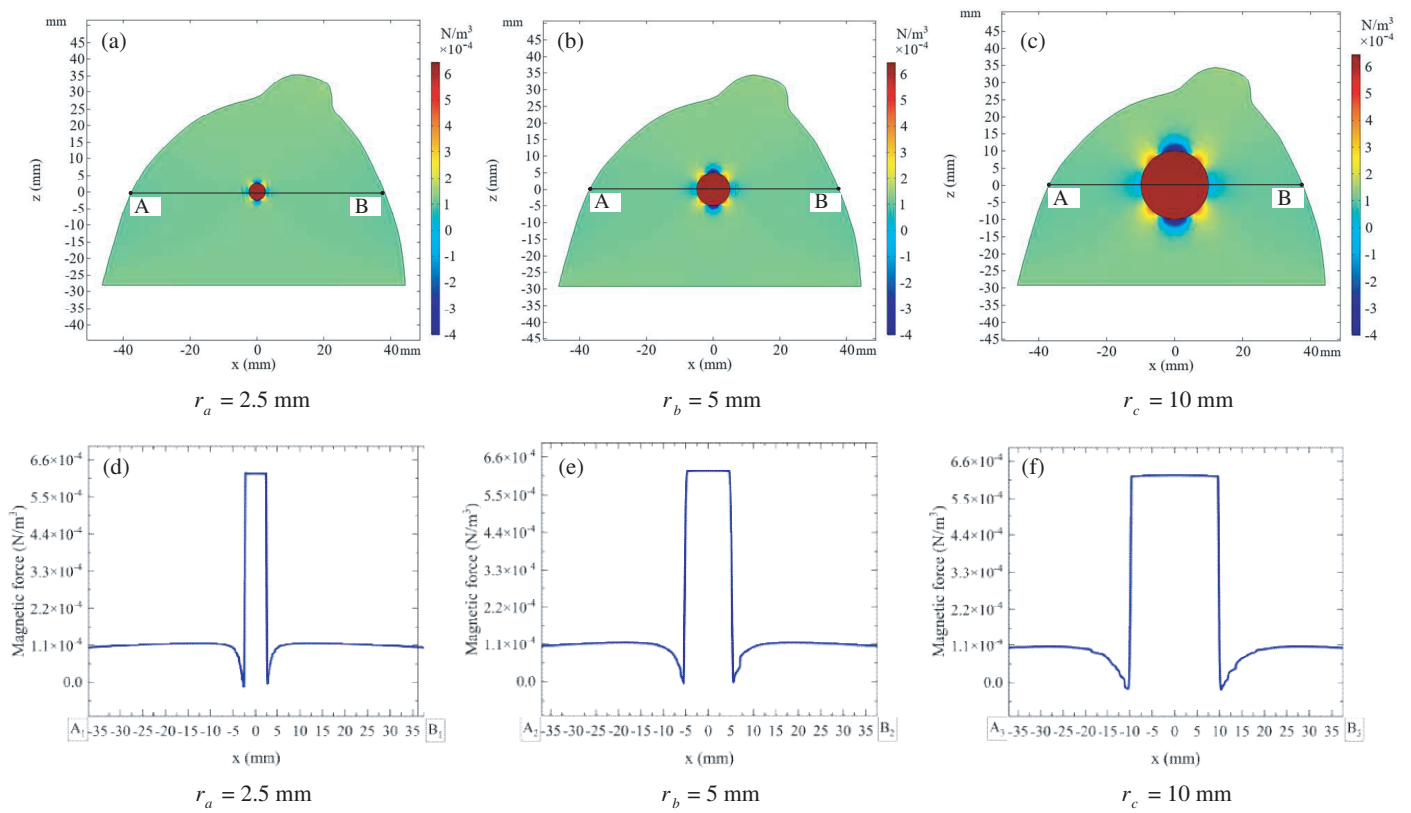

$r_a = 2.5$ mm

$r_b = 5$ mm

$r_c = 10$ mm

$r_a = 2.5$ mm

$r_b = 5$ mm

$r_c = 10$ mm

FIGURE 4. $t = 0.2\,\mu s$ Magnetic simulation data: (a), (b), (c) is the magnetic force distribution map of XOZ section, (d), (e), (f) is the magnetic force distribution curve.

TABLE 1. Related parameters of cylindrical permanent magnet.

Material	Relative permeability	Electric conductivity (S/m)	Radius (mm)	Height (mm)	Spacing (mm)
Ndfeb magnet N50	1.05	1×10^{-16}	120	30	120

TABLE 2. Structural parameters of Maxwell coils.

Outside diameter (mm)	Inside diameter (mm)	Width (mm)	Height (mm)	Turns (mm)	Depth (mm)
90	75	15	4	10	1.5

TABLE 3. EMG 304 specifications.

Parameters	Expressions	Values
Nominal particle diameter	d	10 nm
Density @25 °C	D	1.24×10^3 kg/m^3
Volume fraction	c	4.5%vol
Magnetic susceptibility	χ	5.03
Saturation Magnetization	M_s	2.75×10^5 A/m
Magnetic moment	m	1.45×10^{-19} A·m^2
Number concentration	N	2.01×10^{20}/mL

upper and lower coils of the Maxwell coil are excited by narrow pulse currents of equal magnitude but opposite direction, in order to ensure that there is no reverse polarity oscillation when the current waveform drops to zero. Therefore, the excitation current is set as a sinusoidal attenuation truncated wave signal, $I_S(t) = 3850e^{-5 \times 10^6 t} \sin(10^5 \pi t)$. The current reaches its maximum around 0.2 µs and lasts for 2 µs.

Based on the structural parameters provided in Table 1 and Table 2, the Maxwell coil and cylindrical permanent magnet models are constructed in COMSOL. The three-dimensional model of the breast is imported into the simulation, as depicted in Figure 3. In the simulation, the breast model is utilized to represent the biological tissue, with the magnetic properties of the biological tissue being neglected and the relative permeability set to 1 [17]. Within the breast model, a spherical structure is employed to simulate the cluster of MNPs present in the biological tissue. The parameters of the MNPs are obtained from the water-soluble superparamagnetic nanoparticle EMG304 (Ferrotec (USA) Corporation), and their specifications are detailed in Table 3.

The concentration of MNPs plays a crucial role in determining the magnetic force, as indicated by formula (5). In theory, a higher concentration of MNPs leads to improved imaging effects. However, in practical applications of MACT-MI, which involve in vivo experiments, the concentration of the particle solution must be carefully controlled. Excessively high concentrations can have adverse effects on the patient's physiological functions. According to literature [20], it is necessary to avoid excessively high concentrations of MNPs in actual usage. Moreover, literature [16, 21] reports that the iron content in the EMG 304 solution exceeds the approved limits set by the FDA. Therefore, during the experiments, the MNPs concentration needs to be diluted. In the simulation, the MNPs concentration is set to 1×10^{16}/mL.

By using the parameters provided in Table 3 for EMG 304, the calculation according to formula (2) yields a saturated mag-

netic field strength of $H_s = 1.18 \times 10^5$ A/m. Meanwhile, the magnetic field strength generated by the Maxwell coil-cylindrical permanent magnet in the imaging area is approximately 1.967×10^5 A/m. Therefore, the EMG 304 can achieve a state of saturated magnetization. Subsequently, the magnetic force of MNPs is calculated using formula (5).

4. RESULTS

Conforming to the categorization defined by the American College of Radiology [22], breast tissue can be classified into four categories: Mostly Fatty ($< 25\%$ glandular tissue), Scattered Fibroglandular (25%–50% glandular tissue), Heterogeneously Dense (50%–75% glandular tissue), and Very Dense ($> 75\%$ glandular tissue). The literature [23] shows that breast tumors are more likely to occur in patients with abundant breast glands and uneven dense glands, followed by patients with scattered fibrous and extremely dense glands. Therefore, the breast type used in the simulation study of models with different tumor parameters is uneven dense glands. The electrical and acoustic tissue parameters of the four breast tissues are shown in Table 4 [24, 25].

The spherical tumor tissue (which is defined as benign tumor in this paper) is constructed in the model, and the simulation research is carried out for the two parameters of the radius and position of the tumor and four different breast tissues. At the same time, a malignant tumor model was also constructed, including ellipsoidal, irregular and needle-like tumors. A total of 11 tumor breast models with different parameters were obtained, and the magnetic force and sound pressure were calculated in turn. The specific parameter settings of the model are shown in Table 4. Building upon the theoretical foundation elucidated in Section 2 and the comprehensive simulation model presented in Section 3, this study embarks on a simulation-based analysis, encompassing four distinct MACT-MI models.

TABLE 4. Breast models with different parameters.

Model		Breast tissue	Relative Permittivity	Conductivity (S/m)	Density (kg/m^3)	Velocity (m/s)	Tumor radius (mm)	Tumor location (mm)	Tumor shape
Different radii	Model 1	Heterogeneously Dense	44.31	1.7103	1003.3	1525.3	2.5	(0, 0, 0)	
	Model 2	Heterogeneously Dense	44.31	1.7103	1003.3	1525.3	5	(0, 0, 0)	
	Model 3	Heterogeneously Dense	44.31	1.7103	1003.3	1525.3	10	(0, 0, 0)	Sphere
Different location	Model 4	Heterogeneously Dense	44.31	1.7103	1003.3	1525.3	5	(−15, 0, −15)	
	Model 5	Heterogeneously Dense	44.31	1.7103	1003.3	1525.3	5	(15, 0, 15)	
Different Breast tissue	Model 6	Mostly Fatty	2.53	0.011	928	1436	5	(0,0,0)	
	Model 7	Scattered Fibroglandular	23.42	0.8606	965.6	1480.6	5	(0,0,0)	
	Model 8	Very Dense	65.2	2.56	1041	1570	5	(0, 0, 0)	
Malignant Tumor	Model 9	Heterogeneously Dense	44.31	1.7103	1003.3	1525.3	5,4,4	(0, 0, 0)	Ellipsoid
	Model 10	Heterogeneously Dense	44.31	1.7103	1003.3	1525.3		(0, 0, 0)	Irregular
	Model 11	Heterogeneously Dense	44.31	1.7103	1003.3	1525.3	6.5	(0, 0, 0)	Needle

4.1. Models of Different Tumor Radius

The parameters of the breast tissue were established based on the specifications outlined in Table 1. The tumor was positioned at the center with coordinates (0, 0, 0) (unit: mm), and the tumor radius was varied, specifically set as $r_a = 2.5$ mm, $r_b = 5$ mm, and $r_c = 10$ mm. This resulted in the creation of Model 1, Model 2, and Model 3. The magnetic distribution and sound pressure distribution in the XOZ section were calculated for these models. To investigate the changes in magnetic force and sound pressure under different tumor size conditions, the XOZ plane's cross-section was selected. At 0.2 μs, the magnetic force curve was plotted, while at 1 μs, the sound pressure curve was generated. The coordinates for the starting and ending points A$_1$ (A$_2$, A$_3$) and B$_1$ (B$_2$, B$_3$) were (−37, 0, 0) and (37.5, 0, 0), respectively (unit: mm). The coordinates for points C$_1$ (C$_2$, C$_3$) and D$_1$ (D$_2$, D$_3$) were (0, 0, 27.5) and (0, 0, −29) respectively (unit: mm).

As depicted in Figure 4, it is evident that the magnetic force is concentrated within the tumor tissue encapsulated by MNPs, and the width of the wavefront of the magnetic force corresponds to the diameter of the tumor. Furthermore, a significant alteration in the magnetic force is observed at the boundary between the tumor and the breast tissue, which can be attributed to the change in magnetic particle concentration at this interface. The distribution of sound pressure is presented in Figure 5. The sound pressure exhibits substantial variations at the upper and lower edges of the tumor tissue, while demonstrating relatively uniform distribution along the z-direction. As a result of the

dipole sound source characteristics, the sound pressure exhibits symmetrical distribution in opposite directions. Notably, forward and reverse peaks of sound pressure are manifested within the tumor encapsulated by MNPs. The peak pulse width corresponds to the tumor radius, thereby enabling the sound pressure distribution to reflect the size information of the tumor. Despite the reduced tumor radius, the peak amplitude and peak pulse width of the sound pressure curve diminish; nevertheless, even in Figure 5(d) depicting the smallest tumor radius, the distinctions remain clearly distinguishable.

4.2. Models of Different Tumor Center Positions

Based on the parameters specified in Table 1, the breast tissue parameters were configured accordingly. A tumor with a radius of 5 mm was positioned at different center coordinates: (−15, 0, −15), (0, 0, 0), and (15, 0, 15) (unit: mm). This led to the creation of Model 4, Model 2, and Model 5, which were utilized to calculate the magnetic distribution and sound pressure distribution within the XOZ section. To investigate the effects of tumor location on the magnetic force and sound pressure, an intercept line was selected on the XOZ plane. The magnetic force curve at 0.2 μs and the sound pressure curve at 2 μs were plotted. The starting and ending points on the intercept line were denoted as A$_4$, A$_2$, and A$_5$, with coordinates (−42, 0, −15), (−37, 0, 0), and (−25, 0, 15), respectively (unit: mm). The corresponding coordinates for the ending points were labeled as B$_4$, B$_2$, and B$_5$, with values (42, 0, −15), (37.5, 0, 0), and (30, 0, 15), respectively (unit: mm). Additionally, the
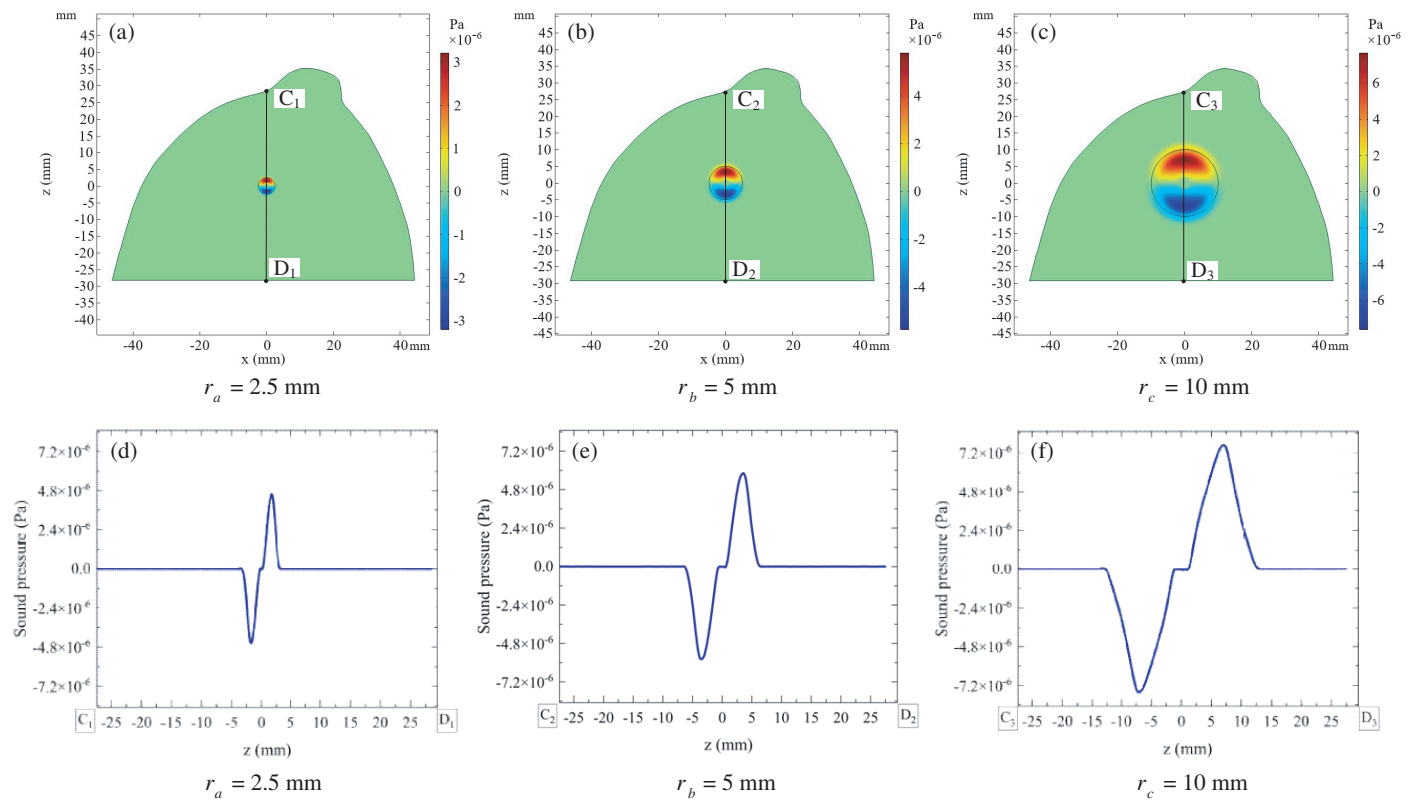
FIGURE 5. $t = 1\,\mu s$ sound pressure simulation data: (a), (b), (c) is the sound pressure distribution map of XOZ section, (d), (e), (f) is the sound pressure distribution curve.

coordinates for points C_4, C_2, and C_5 were $(-15, 0, 22)$, $(0, 0, 27.5)$, and $(15, 0, 33)$, respectively (unit: mm), while the coordinates for points D_4, D_2, and D_5 were $(-15, 0, -29)$, $(0, 0, -29)$, and $(15, 0, -29)$, respectively (unit: mm).

As depicted in Figure 6, it is evident that the distribution of magnetic force varies according to the tumor location, allowing for the determination of the specific tumor location based on the peak position of the magnetic waveform. Figure 7 illustrates significant changes in the distribution of sound pressure, with the forward and reverse peaks of sound pressure shifting in phase with the alteration in tumor location. In summary, the waveform distribution of both magnetic force and sound pressure can serve as a means to map the tumor location. This suggests that in the diagnosis and treatment of breast tumors, the specific tumor location can be confirmed through the magnetic acoustic signal of MNPs, enabling the monitoring of tumor metastasis.

4.3. Models of Different Breast Tissues

Considering the parameters outlined in Table 1, a tumor with a radius of 5 mm was positioned at the center coordinates $(0, 0, 0)$ (unit: mm). Utilizing the electrical and acoustic parameters specified for different breast types in Table 3, Model 2, Model 6, Model 7, and Model 8 were established to calculate the distribution curves of magnetic force and sound pressure within the XOZ section. The starting and ending points A_6, A_7, A_2, and A_8, as well as B_6, B_7, B_2, and B_8, shared the coordinates $(-37, 0, 0)$ and $(37.5, 0, 0)$ (unit: mm). Furthermore, the co-

ordinates for points C_6, C_7, C_2, and C_8 were $(0, 0, 27.5)$ (unit: mm), while the coordinates for points D_6, D_7, D_2, and D_8 were $(0, 0, -29)$ (unit: mm). In Figures 8 and 9, the subpanel (b) is a zoomed in view of the boxed are in subpanel (a).

From the analysis presented in Figure 8 and Figure 9, it is apparent that the variation in breast tissue types does not significantly impact the distribution of magnetic force and sound pressure. Despite the wide range of electrical and acoustic parameter variations among the four different breast tissues, the waveform changes observed in the magnetic force and sound pressure still provide information regarding the tumor boundary position.

To observe the distribution differences of magnetic force and sound pressure in various breast tissues, the paper specifically focuses on the magnetic force distribution within the tumor center range of $x = -3\,mm$ to $x = 3\,mm$, as shown in Figure 8(b). It is notable that within this area, the extremely dense breast tissue exhibits the highest magnetic force, while the fatty breast tissue demonstrates the lowest. This outcome can be attributed to the relationship between magnetic force and the conductivity parameters of breast tissue. The distribution order of magnetic force aligns with the order of conductivity parameters in the breast tissue.

In Figure 9(b), the sound pressure distribution at the tumor boundary positions of $z = 4.8\,mm$ and $z = 5.1\,mm$ is observed. It is observed that the extremely dense breast tissue again displays the highest sound pressure. This finding is linked to the size of the sound velocity parameters in the breast tissue,
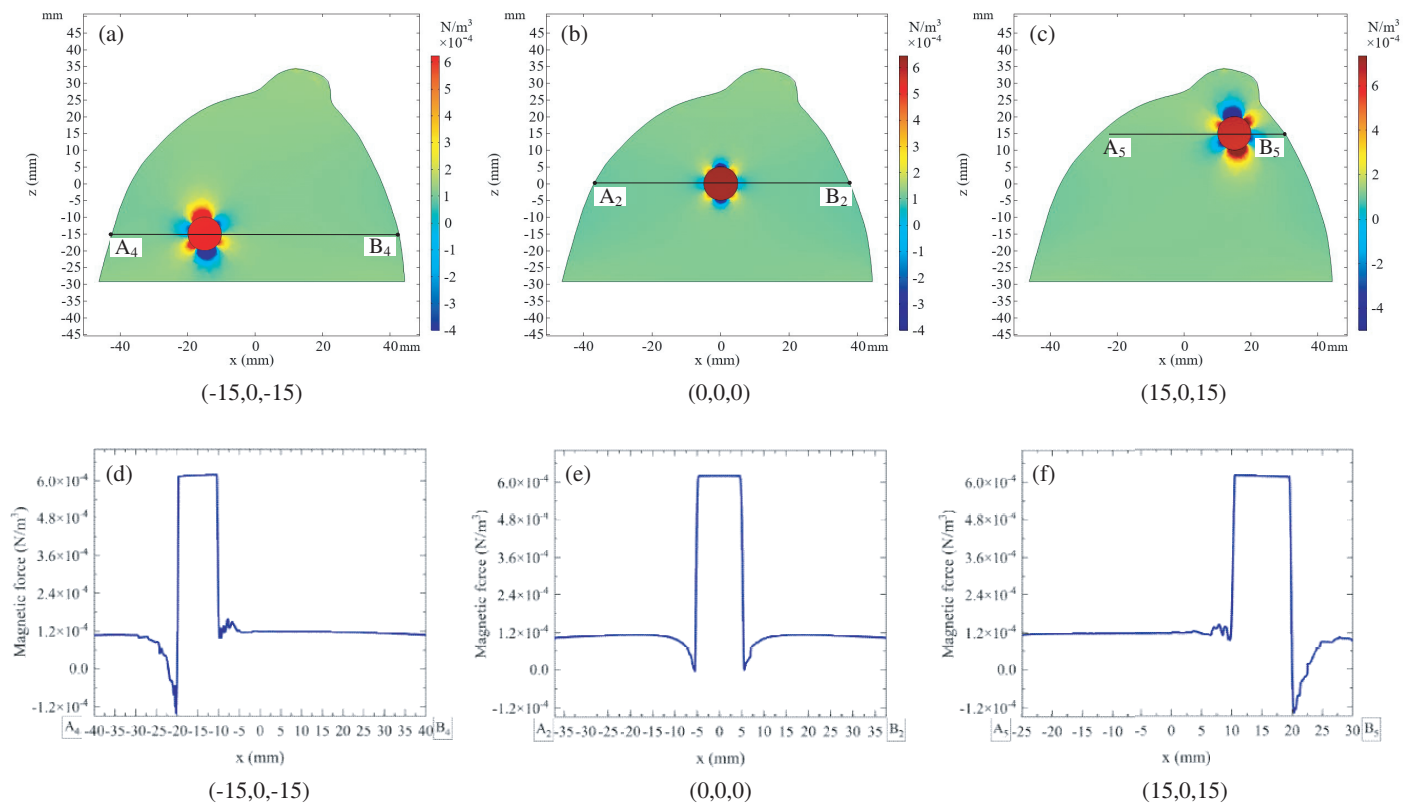
FIGURE 6. $t = 0.2\,\mu s$ magnetic simulation data: (a), (b), (c) is the magnetic force distribution map of XOZ section, (d), (e), (f) is the magnetic force distribution curve.
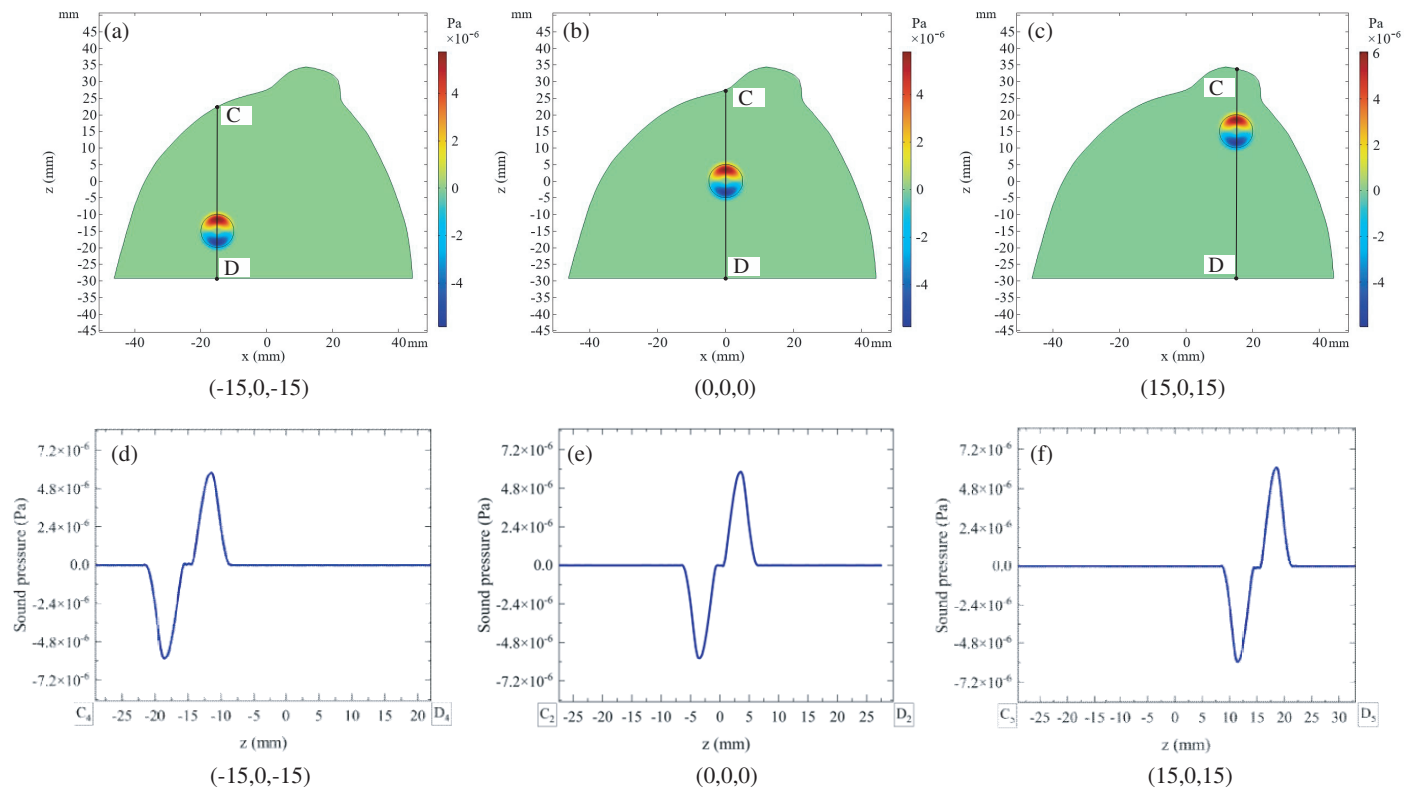

FIGURE 7. $t = 2\,\mu s$ sound pressure simulation data: (a), (b), (c) is the sound pressure distribution map of XOZ section, (d), (e), (f) is the sound pressure distribution curve.
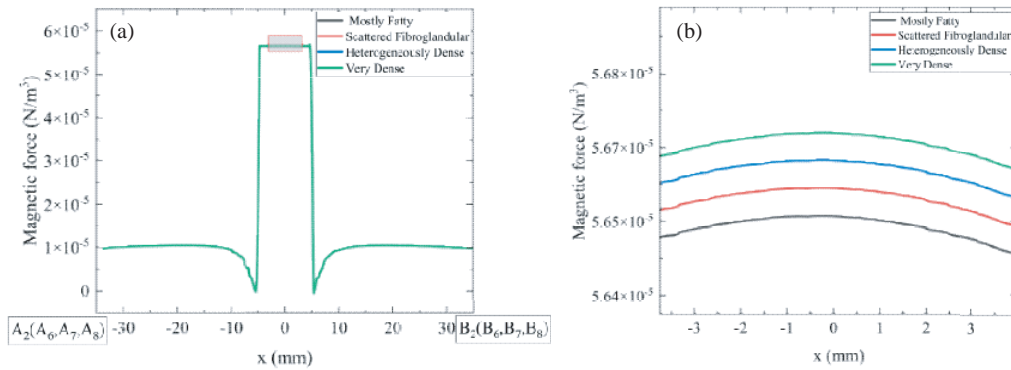
FIGURE 8. $t = 0.2\,\mu s$ magnetic simulation data: (a) Magnetic force distribution curve; (b) $(-3, 3)$ Magnetic force distribution curve.
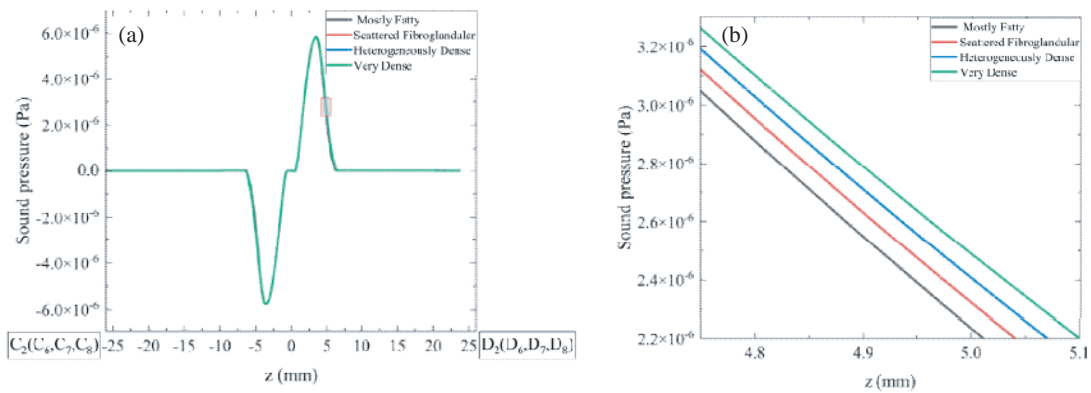

FIGURE 9. $t = 2\,\mu s$ sound pressure simulation data: (a) Sound pressure distribution curve; (b) $(4.8, 5.1)$ Sound pressure distribution curve.

FIGURE 10. Experimental model of tumor.

as the magnitude of sound pressure is influenced by these parameters. The distribution order of sound pressure corresponds to the order of the sound velocity parameters within the breast tissue.

4.4. Model of Malignant Tumor

Based on findings presented in the literature [26], it is established that benign and malignant tumors can be differentiated based on their distinct structural characteristics. Benign tumors typically exhibit a round shape with clearly defined edges, while malignant tumors, conversely, lack well-defined boundaries, often presenting irregular, lobulated, or needle-like edges. To facilitate experimental comparisons, the authors de-

vised a tumor model, as illustrated in Figure 10. On this basis, in order to further explore the influence of tumor structure, this study introduced three different tumor models: ellipsoid tumor, irregular tumor, and needle-shaped tumor, and defined the latter two as malignant tumors.

As depicted in Figure 11, the ellipsoid tumor is characterized by short and middle radii measuring 4 mm each, with a long radius of 5 mm. The needle-shaped tumor model features a middle spherical section with a radius of 4 mm, extending to a maximum radius of 6.5 mm to emulate its needle-like configuration. To simulate the specific needle-like shape of the tumor, a cone was employed, featuring the following parameters: a radius of 1 mm, height of 2.5 mm, with eight cones positioned around the spherical core. The irregular tumor, on the other hand, corre-
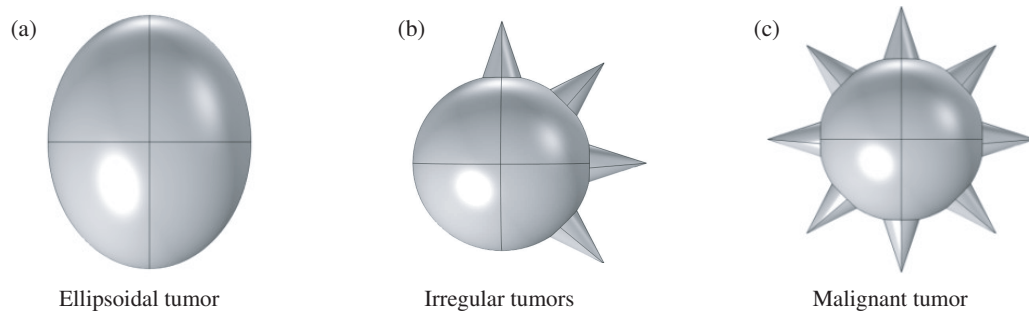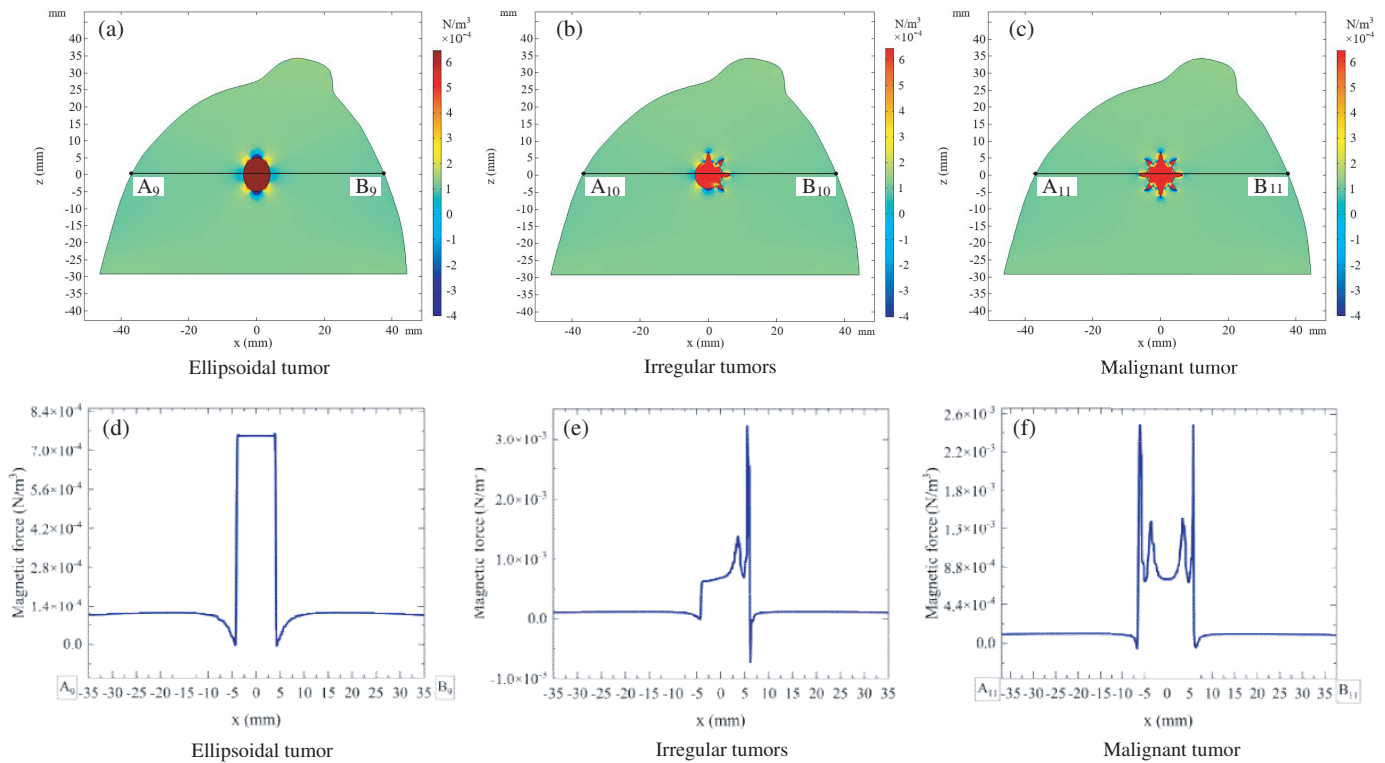
FIGURE 11. Tumor model.

FIGURE 12. $t = 0.2\,\mu\text{s}$ magnetic simulation data: (a), (b), (c) is the magnetic force distribution map of XOZ section, (d), (e), (f) is the magnetic force distribution curve.

sponds to a needle-shaped tumor with only four cones remaining, as depicted in Figure 11(b).

Following this, the malignant tumor models were seamlessly integrated into the MACT-MI simulation framework. The distribution curves pertaining to magnetic force and sound pressure were generated by capturing the intercept line, facilitating a comprehensive analysis of their respective variation patterns. It is worth noting that the coordinates of the intercept line are delineated as follows: A_9, A_{10}, A_{11}, and B_9, B_{10}, B_{11} have coordinates of $(-37, 0, 0)$ and $(37.5, 0, 0)$, respectively. Additionally, C_9, C_{10}, C_{11}, and D_9, D_{10}, D_{11} are positioned at $(0, 0, 27.5)$ and $(0, 0, -29)$, respectively (units: mm). The simulation outcomes of these three models were subsequently compared and examined, thereby enabling an in-depth assessment of the impact of tumor structure on both magnetic force and sound pressure distributions.

The insights drawn from Figure 12 reveal that the magnetic distribution within the three breast tumor models remains predominantly concentrated within the tumor region. The relative positioning of the tumor in relation to the breast tissue can be effectively distinguished through the localization of magnetic mutations. Notably, the magnetic distribution pattern of ellipsoidal tumors closely resembles that of benign tumors, characterized by a magnetic force mutation primarily at the tumor boundary. However, compared to irregular tumors and malignant tumors, it becomes evident that variations in tumor shape exert a discernible impact on the magnetic force distribution. In irregular tumors, in addition to the tumor-to-breast tissue boundary, magnetic mutations also occur at the interface between the spherical and conical sections of the tumor. The magnetic concentration within the conical region aligns closely with
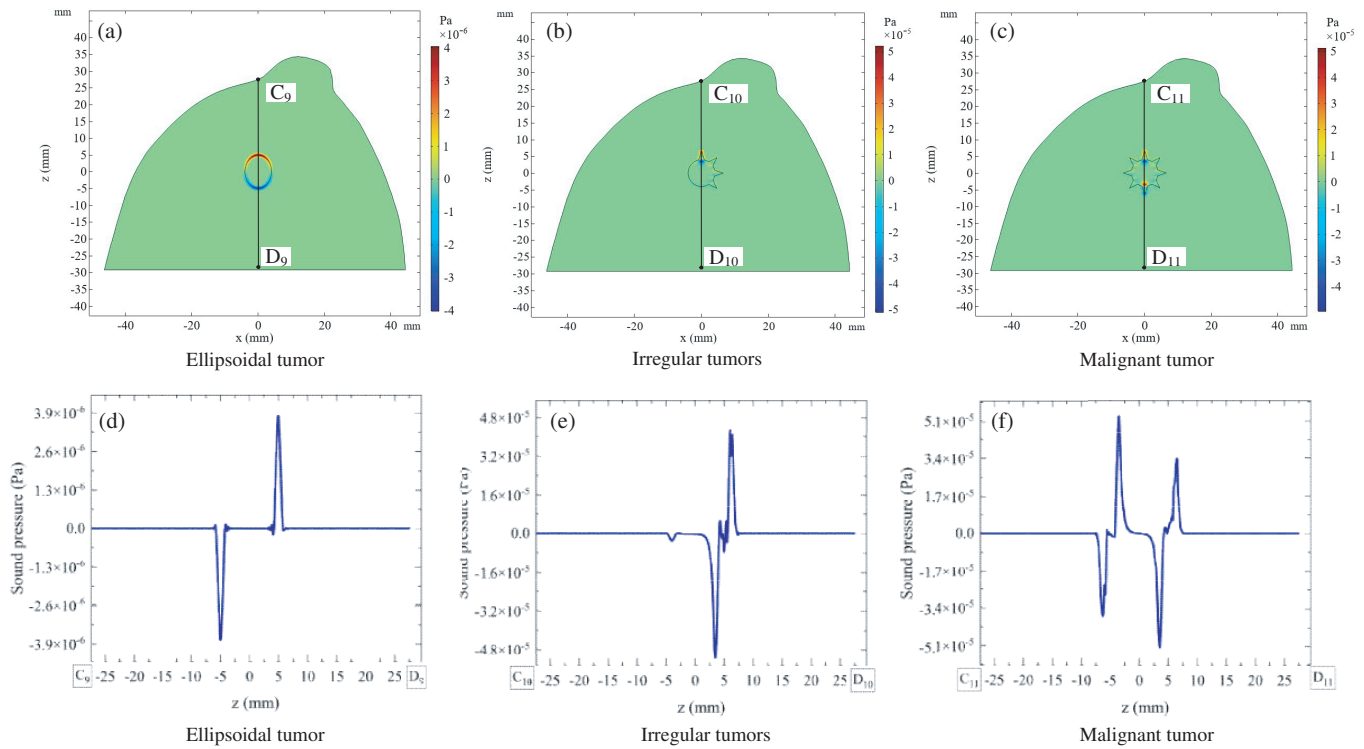
FIGURE 13. $t = 0.5\,\mu s$ sound pressure simulation data: (a), (b), (c) is the sound pressure distribution map of XOZ section, (d), (e), (f) is the sound pressure distribution curve.

that of the spherical area, with variations primarily attributed to changes in tumor shape.

Likewise, the sound pressure distribution of ellipsoid tumors exhibits a resemblance to that of benign tumors, with relatively minor disparities. However, in the case of irregular tumors and needle-shaped tumors, the sound pressure distribution markedly deviates from that of benign tumors. As illustrated in Figure 13, it is noteworthy that the location of sound pressure anomalies correlates with the magnetic force distribution. For ellipsoid and benign tumors, both the magnetic force and sound pressure exhibit relatively consistent patterns and are symmetrically distributed in opposite directions.

Comparative analysis of the magnetic force and sound pressure distribution between benign and malignant tumors leads to the observation that benign tumors possess a smoother surface, resulting in magnetic force and sound pressure anomalies primarily occurring at the tumor's interface with surrounding breast tissue. Within the tumor, the distribution tends to remain relatively uniform. Conversely, in the case of needle-shaped malignant tumors, the surface exhibits irregularities, leading to magnetic force and sound pressure anomalies manifesting within the magneto-acoustic signal inside the tumor. It is worth noting that the complexity of the tumor structure corresponds to the extent of magneto-acoustic signal anomalies. Furthermore, the peak magnetic force observed at the tip of the needle-shaped malignant tumors is notably greater. This example serves as a foundation and a potential diagnostic indicator for distinguishing between benign and malignant tumors.

5. DISCUSSION AND CONCLUSIONS

In this study, we constructed a three-dimensional model representing a real breast. Utilizing various parameters for different tumors and breast tissues, we established four distinct MACT-MI simulation models, encompassing variations in tumor size, position, breast tissue characteristics, and benign and malignant tumor types. We subsequently performed computations to address specific research questions and obtained two-dimensional distribution plots and one-dimensional variation curves depicting magnetic force and sound pressure. The primary focus of our investigation was to explore the impact of changes in breast model parameters on the distribution of magnetic force and sound pressure. Key findings from our study include:

(1) Magnetic field and acoustic pressure distributions can be employed to map the size and spatial information of tumors, thereby confirming the feasibility of monitoring tumor activities through the surveillance of magnetic nanoparticles.

(2) Different breast types have little impact on the distribution patterns of magnetism and sound pressure. In all four distinct breast tissue types, it is possible to utilize the magnetic-acoustic signals generated by MNPs in an alternating magnetic field to ascertain the tumor's positional information, thus establishing a fundamental prerequisite for targeted precision therapy of tumors using drug-loaded magnetic particles.

(3) Comparing spherical, ellipsoid, irregular, and malignant tumors, it can be seen that the structure of the tumor will affect the distribution and amplitude of magnetic force and sound pressure. Smooth tumors exhibit a more regular magnetoacous-

tic signal distribution, with mutations occurring solely at the tumor boundary. In contrast, needle-like tumors demonstrate higher magnetic force and sound pressure amplitudes.

(4) Malignant tumors, due to their complex internal structures, exhibit multiple oscillations in magnetic and sound pressure signals within the tumor. This observation carries significant implications for distinguishing between benign and malignant tumors.

References [27, 28] underscore the use of breast MRI tomographic images to construct a realistic three-dimensional breast model and investigate the MAT-MI forward problem based on this model. The outcomes highlight significant deviations in eddy current density distribution and sound source amplitude compared to the ideal double-layer concentric sphere model, emphasizing the utility of real breast models in obtaining more realistic simulation data. Historically, MACT-MI research predominantly concentrated on magnet systems and frequently employed regular models such as ideal spheres, cubes, and cylinders [9, 10, 19]. However, the intricate external morphology of biological organs like the breast and liver necessitates model fidelity to advance MACT-MI research and clinical applications. MACT-MI benefits from its capacity to exploit differences in magnetic properties between MNPs and surrounding tissues, resulting in high resolution and contrast [17]. This capability effectively reflects variations in magnetic characteristics between biological tissues and magnetic nanoparticles. Moreover, the sensitivity of magnetic field changes in MNPs, compared to conductivity changes in diseased tissue, enables the monitoring of tumor cells through magnetic particle tracking.

It is worth noting that our numerical calculations of magnetic and sound fields assume uniform sound velocity, while biological tissues in practice exhibit nonuniform sound velocity profiles. Additionally, our breast model captures only the basic shape of the real breast without considering internal structures or precise parameter settings for different tissues such as skin, fat, and breast. These simplifications are inherent in the establishment of simulation models and the execution of forward problem calculations. Future research endeavors will aim to optimize the simulation model and address existing limitations.

In conclusion, this study successfully addresses the MACT-MI forward problem using a real breast model. The distribution of magnetic force and sound pressure effectively reveals tumor size, location, and benign or malignant characteristics. Consequently, MACT-MI holds promising prospects for applications in breast tumor monitoring and targeted therapy.

DECLARATION OF COMPETING INTEREST

We declare that we have no financial and personal relationships with other people or organizations that can inappropriately influence our work. There is no professional or other personal interest of any nature or kind in any product, service and/or company that could be construed as influencing the position presented in, or the review of, the manuscript entitled "Simulation Analysis of Breast Tumor Model Based on Magneto-acoustic Concentration Tomography with Magnetic Induction".

REFERENCES

[1] Kianfar, E., "Magnetic nanoparticles in targeted drug delivery: A review," *Journal of Superconductivity and Novel Magnetism*, Vol. 34, No. 7, 1709–1735, Jul. 2021.

[2] Li, Z., W. Wan, Z. Bai, B. Peng, X. Wang, L. Cui, Z. Liu, K. Lin, J. Yang, J. Hao, and F. Tian, "Construction of ph-responsive nanoplatform from stable magnetic nanoparticles for targeted drug delivery and intracellular imaging," *Sensors and Actuators, B: Chemical*, Vol. 375, 132869, Jan. 2023.

[3] Yang, H., F. Jiang, L. Zhang, L. Wang, Y. Luo, N. Li, Y. Guo, Q. Wang, and J. Zou, "Multifunctional l-arginine-based magnetic nanoparticles for multiple-synergistic tumor therapy," *Biomaterials Science*, Vol. 9, No. 6, 2230–2243, Mar. 2021.

[4] Taherian, A., N. Esfandiari, and S. Rouhani, "Breast cancer drug delivery by novel drug-loaded chitosan-coated magnetic nanoparticles," *Cancer Nanotechnology*, Vol. 12, No. 1, Dec. 2021.

[5] Harvell-Smith, S., L. D. Tung, and N. T. K. Thanh, "Magnetic particle imaging: Tracer development and the biomedical applications of a radiation-free, sensitive, and quantitative imaging modality," *Nanoscale*, Vol. 14, No. 10, 3658–3697, Mar. 2022.

[6] Park, S.-J., S. R. Han, Y. H. Kang, E.-J. Lee, E.-G. Kim, H. Hong, J.-C. Jeong, M.-S. Lee, S.-H. Lee, and D.-Y. Song, "In vivo preclinical tumor-specific imaging of superparamagnetic iron oxide nanoparticles using magnetic particle imaging for cancer diagnosis," *International Journal of Nanomedicine*, Vol. 17, 3711–3722, 2022.

[7] Senthilkumar, N., P. K. Sharma, N. Sood, and N. Bhalla, "Designing magnetic nanoparticles for in vivo applications and understanding their fate inside human body," *Coordination Chemistry Reviews*, Vol. 445, 214082, Oct. 2021.

[8] Lu, C., L. Han, J. Wang, J. Wan, G. Song, and J. Rao, "Engineering of magnetic nanoparticles as magnetic particle imaging tracers," *Chemical Society Reviews*, Vol. 50, No. 14, 8102–8146, Jul. 2021.

[9] Shi, X., G. Liu, X. Yan, and Y. Li, "Simulation research on magneto-acoustic concentration tomography of magnetic nanoparticles with magnetic induction," *Computers in Biology and Medicine*, Vol. 119, 103653, Apr. 2020.

[10] Yan, X., Y. Pan, W. Chen, Z. Xu, and Z. Li, "Simulation research on the forward problem of magnetoacoustic concentration tomography for magnetic nanoparticles with magnetic induction in a saturation magnetization state," *Journal of Physics D: Applied Physics*, Vol. 54, No. 7, 075002, 2020.

[11] Arnold, M., E. Morgan, H. Rumgay, A. Mafra, D. Singh, M. Laversanne, J. Vignat, J. R. Gralow, F. Cardoso, S. Siesling, and I. Soerjomataram, "Current and future burden of breast cancer: Global statistics for 2020 and 2040," *Breast*, Vol. 66, 15–23, Dec. 2022.

[12] Jung, K. O., H. Jo, J. H. Yu, S. S. Gambhir, and G. Pratx, "Development and mpi tracking of novel hypoxia-targeted theranostic exosomes," *Biomaterials*, Vol. 177, 139–148, Sep. 2018.

[13] Wang, G., W. Li, G. Shi, Y. Tian, L. Kong, N. Ding, J. Lei, Z. Jin, J. Tian, and Y. Du, "Sensitive and specific detection of breast cancer lymph node metastasis through dual-modality magnetic

particle imaging and fluorescence molecular imaging: A preclinical evaluation," *European Journal of Nuclear Medicine and Molecular Imaging*, Vol. 49, No. 8, 2723–2734, Jul. 2022.

[14] Parkins, K. M., K. P. Melo, Y. Chen, J. A. Ronald, and P. J. Foster, "Visualizing tumour self-homing with magnetic particle imaging," *Nanoscale*, Vol. 13, No. 12, 6016–6023, Mar. 2021.

[15] Zhu, X., J. Li, P. Peng, N. H. Nassab, and B. R. Smith, "Quantitative drug release monitoring in tumors of living subjects by magnetic particle imaging nanocomposite," *Nano Letters*, Vol. 19, No. 10, 6725–6733, Oct. 2019.

[16] Yan, X., Z. Li, D. Sun, W. Chen, and P. Gao, "Magnetoacoustic concentration tomography of magnetic nanoparticles with magnetic induction based on matrix coil," *Transactions of China Electrotechnical Society*, Vol. 37, No. 17, 4269–4283, 2022.

[17] Yan, X.-H., Y. Zhang, and G.-Q. Liu, "Simulation research on effect of magnetic nanoparticles on physical process of magneto-acoustic tomography with magnetic induction," *Chinese Physics B*, Vol. 27, No. 10, 104302, 2018.

[18] Liu, G. Q., *Magnetoacoustic Tomography Technology*, Science Press, 2014.

[19] Yan, X., Z. Li, Y. Pan, *et al.*, "Simulation of the influence of permanent magnets of the same polarity on the magneto-acoustic concentration tomography of magnetic nanoparticles with magnetic induction process," *Transactions of China Electrotechnical Society*, Vol. 37, No. 8, 1926–1937, 2022.

[20] Sun, C., J. S. H. Lee, and M. Zhang, "Magnetic nanoparticles in mr imaging and drug delivery," *Advanced Drug Delivery Reviews*, Vol. 60, No. 11, 1252–1265, Aug. 2008.

[21] Hu, G. and B. He, "Magnetoacoustic imaging of magnetic iron oxide nanoparticles embedded in biological tissues with microsecond magnetic stimulation," *Applied Physics Letters*, Vol. 100, No. 1, 3741–3743, Jan. 2012.

[22] D'Orsi, C., L. Bassett, S. Feig, *et al.*, *Breast Imaging Reporting and Data System (BI-RADS ®)*, 4th ed., American College of Radiology, 2003.

[23] Bao, W., X. Shen, X. Zheng, *et al.*, "A study on the correlation between breast lump, breast density and radiation dose in mammography," *Oncoradiology*, Vol. 31, No. 6, 581–585, 2022.

[24] Wang, X., T. Qin, R. S. Witte, and H. Xin, "Computational feasibility study of contrast-enhanced thermoacoustic imaging for breast cancer detection using realistic numerical breast phantoms," *IEEE Transactions on Microwave Theory and Techniques*, Vol. 63, No. 5, 1489–1501, May 2015.

[25] Zastrow, E., S. K. Davis, M. Lazebnik, F. Kelcz, B. D. Van Veen, and S. C. Hagness, "Database of 3D grid-based numerical breast phan-toms for use in computational electromagnetics simulations," Department of Electrical and Computer Engineering University of Wisconsin-Madison, 2008.

[26] Martins, R. A., J. M. Felicio, J. R. Costa, and C. A. Fernandes, "Systematic analysis of microwave breast imaging detection of different-sized malignant and benign tumors," in *2022 16th European Conference on Antennas and Propagation (EuCAP)*, 1–4, Madrid, Spain, Mar. 2022.

[27] Zhang, S., W. Hou, X. Zhang, *et al.*, "Forward problem in magnetoacoustic tomography with magnetic induction based on real model of breast," *Transactions of China Electrotechnical Society*, Vol. 31, No. 24, 126–133, 2016.

[28] Hou, W., S. Zhang, Z. Wang, and G. Xu, "The study of magnetoacoustic tomography with magnetic induction through vector source reconstruction based on real model of breast," in *2016 Asia-Pacific International Symposium on Electromagnetic Compatibility (APEMC)*, 862–864, Shenzhen, China, May 2016.